Scientific Research Publishing

Geomaterials, 2023, 13, 1-22
https://www.scirp.org/journal/gm
ISSN Online: 2161-7546
ISSN Print: 2161-7538

Integrated Structure and Mineralization Study Using Aero-Magnetic, Aero-Spectrometric and Remote Sensing Data at Esh El-Mallaha Area, Eastern Desert, Egypt

Ahmed A. Elhusseiny

Nuclear Materials Authority, Cairo, Egypt
Email: ahmednoureldin1985@gmail.com

How to cite this paper: Elhusseiny, A.A. (2023) Integrated Structure and Mineralization Study Using Aero-Magnetic, Aero-Spectrometric and Remote Sensing Data at Esh El-Mallaha Area, Eastern Desert, Egypt. *Geomaterials*, **13**, 1-22.
https://doi.org/10.4236/gm.2023.131001

Received: October 2, 2022
Accepted: November 11, 2022
Published: November 14, 2022

Abstract

The main scope of this research is to detect geologic structure trends affecting the study area, determine uranium anomalous areas and define alteration zones. Airborne magnetic data were used to detect the geologic structure trends affecting the study area through applying edge detectors such as total horizontal derivative, analytic signal and tilt derivative. The radio-spectrometry data and Landsat image data were used in determining the uranium anomalous areas and alteration zones. The integration between geology, magnetic and Landsat image was applied through constructing lineaments density map for the three data sets resulting in the leading of NW-SE trend all over the area. This integration makes clear that the basement (Red Sea hills), Esh El-mallaha range and G. Zeit are limiting two large basins (West Mallaha and Zeit). In addition, the main areas of uranium enrichment (Duwi formation at Esh El-Mallaha range) are found to be well related to alteration zones.

Keywords

Structure Trends, Uranium Zones, Alteration Zones, Magnetic Analysis, Landsat-8 OLI Image, Esh El-Mallaha Area

1. Introduction

The study area is located at the northern part of the Eastern Desert between latitudes 27˚17'58"N & 27˚59'02"N and longitudes 32˚56'29"E & 33˚44'25"E, covering an area of about 4560 Km^2 (**Figure 1(a)**). The topographic map shows that the western side of the area which represents the Red Sea hills reaches an elevation of 1600 m at G. Giala, while the elevations on the eastern side decrease to 30

meters until we reach the shoreline (Figure 1(b)).

Eastern Desert of Egypt has been considered the main target for mineral resources exploration, which was hosted by Precambrian rocks. There are many researches that concern with mineralization mapping, especially radioactive minerals ([1] [2] [3]). Radioactive anomaly zones are the result of two main reasons; natural lithological distribution and post magmatic processes caused by either hydrothermal solutions and/or dikes factors. Therefore, mineralization zones investigation is mainly done by evaluating lithological units, alteration, and structural features (e.g. [4] [5] [6]). Consequently, the value of integration of remote sensing and geophysical data and its interpretation is fundamental for providing a geological and mineralogical model of the earth's surface [7]. This study aims essentially to deduce the radioactive mineralization zones, the hydrothermal alteration areas and the structure controlling the mineralization.

Satellite image data is used to determine lithologic contacts that may be located on geologic structures and may extend to the subsurface [8]. Hydrothermal alteration zones and potential mineralization areas can be identified using several approaches like band ratios and principal component analysis (PCA) which used commonly in multispectral data like Landsat ([9]-[17]). Band ratios were applied to the multispectral data to identify hydrothermal alteration zones ([17] [18] [19] [20] [21]) because the hydrothermal processes are often related to mineralization which may as a result change the country rocks properties.

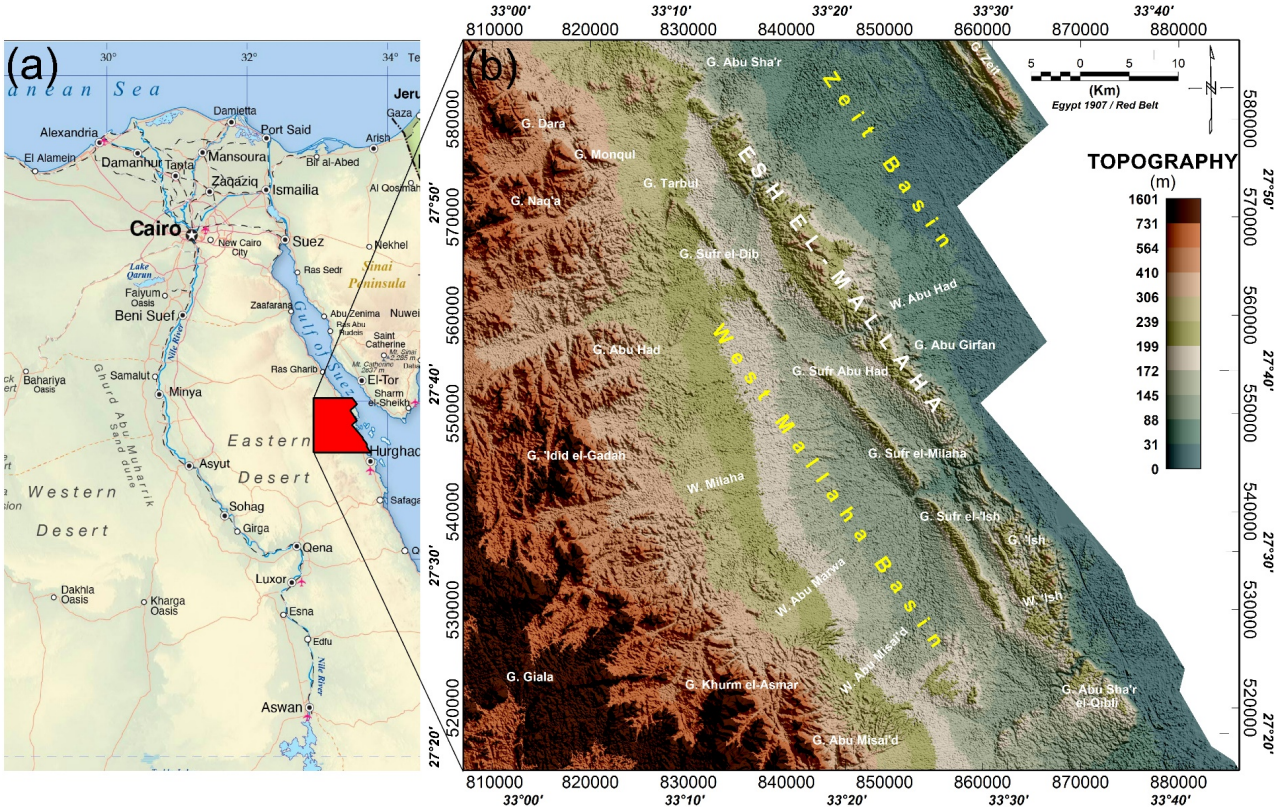

Figure 1. (a) Location map of the study area, (b) Topographic map of the study area.

Airborne magnetic data are usually used in mapping the shallow and deep geologic structures and enlightening intrusions [22]. These structures are represented in trends and intensities on magnetic maps that represent magnetic patterns [23]. The spectrometric maps of the study area will help to locate the high alteration areas of the radioactive minerals and discriminate the boundaries of the different rocks.

2. Geologic Setting

According to [24], the Eastern Desert of Egypt is separated into Northern, Central, and Southern parts depending on the basement characteristics. The area represents part of the Central Eastern Desert of Egypt. The CED was formed by collapse of a small ocean basin or back arc basin [25]. The study area consists of two sedimentary basins (Zeit and West Mallaha basins) trending in the NW-SE direction and lying parallel to the Gulf of Suez [26]. The topographic map (**Figure 1(b)**) showed that the two basins are separated by Esh El-Mallaha heights, which trending NW-SE heading with a height of about 400 m. The geologic map (**Figure 2**) showed that Esh El-mallaha range at the east and red sea hills at the west are bounded by normal faults, trapping West Mallaha basin

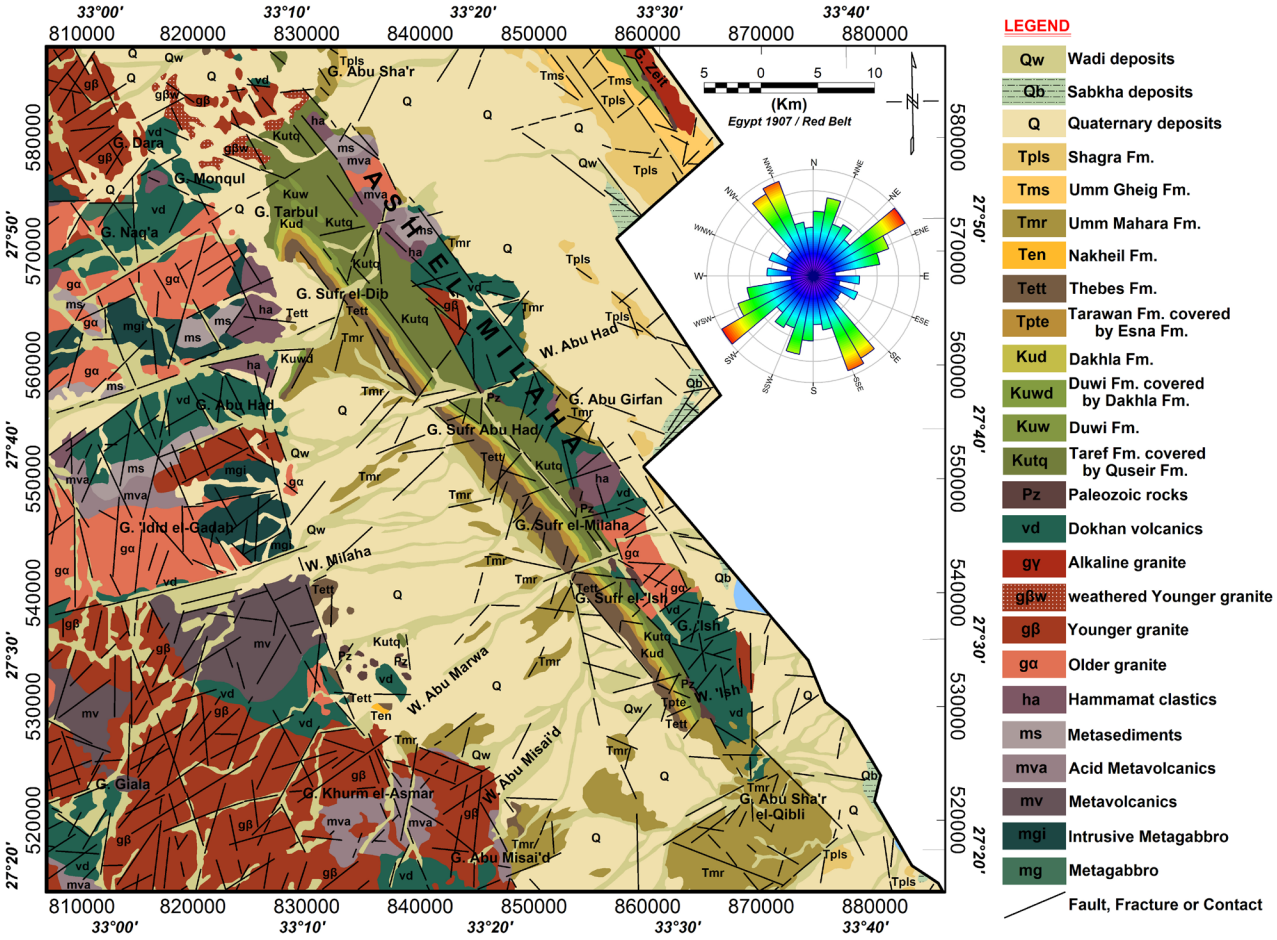

Figure 2. Geologic map of the study area, after conco, 1987.

between them. These normal faults trending mainly in NW-SE direction and in lesser extent in NE-SW direction.

The surface geology is mostly Late Precambrian-Quaternary (**Figure 2**). These rocks are intersected by numerous wadis filled with Quaternary sediments. The western part of the study area is covered by different rock units which can be seen on geological map such as Metamorphic Rocks, Metagabbro, Intrusive Metagabbro, Metavolcanics, Acidic Metavolcanics, Metasediments (a sequence of fine grained "geosynclinals" clastics mostly in a low-grade metamorphism), Hammamat clastics (a thick succession of clastic sediments), Older Granite (felsic plutonic rocks of essentially intermediate composition), Younger Granite (mostly occurs as isolated, equidimensional plutons of 1 to 10 km diameter) and Dokhan Volcanics ([27] [28]). The Upper Cretaceous rocks are represented by Taref, Duwi, and Dakhla formations while the Tertiary rock units are represented by Tarawan, Thebes, Nakheil, Um Mahara, Um Gheig and Shagra formations [29]. Quaternary and Wadi deposits are mainly pebbles of sand, detritus, cobbles and little boulders filling the main wadis. These sediments result mainly from the weathered adjacent rocks of the Red Sea Mountains. The basement rocks are unconformably overlain by the Upper Cretaceous and Tertiary rocks.

3. Data and Methodology

Many data have been used in this research, such as airborne magnetic survey data, airborne radio-spectrometric survey data, in addition to remote sensing data. The magnetic and spectrometry data were acquired along flight lines extending in NE-SW direction with 1.5 km spacing, while the tie lines were flown along profiles perpendicular to the flight lines (NW-SE) with 10 km spacing. The nominal flying altitude was 120 m above ground level [30].

Multispectral remote sensing data, specifically Landsat-8 OLI satellite image has been used as one of the primary data sources. This image was obtained on August 18, 2021, from path 175 and row 041. It was downloaded from the USGS Earth Explorer data portal (https://earthexplorer.usgs.gov/).

3.1. Magnetic Data

The regional gradient of earth's magnetic field was obtained by eliminating the International Geomagnetic Reference Field from the total intensity magnetic data [31]. The final total magnetic intensity data was gridded and presented in **Figure 3**.

The TMI data were reduced to the north magnetic pole (RTP) to overcome the distortion in shape and location produced by the dipolarity problem [32] and presented in **Figure 4**. The RTP map clearly shows the signature of the two basins (Zeit and West Mallaha basins) which have magnetic intensity ranging from −388 to −589 nT and trending NW-SE direction. The basement intrusions at the western part (Red Sea hills) and Esh El-mallaha range at the eastern part exhibit high positive anomalies reach about 650 nT.

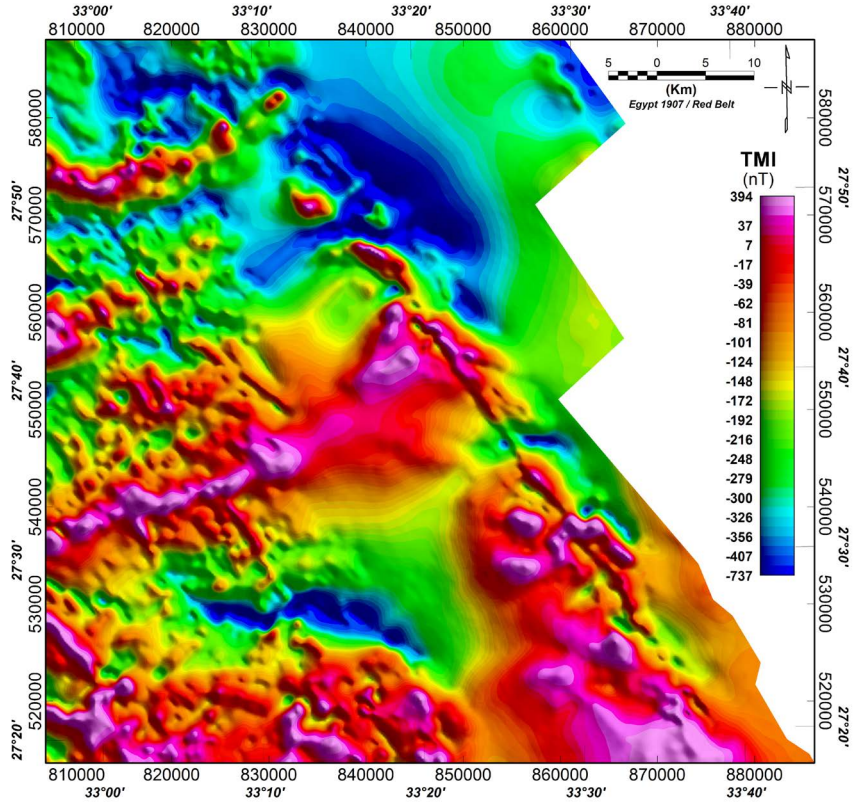

Figure 3. Total magnetic intensity map of the study area.

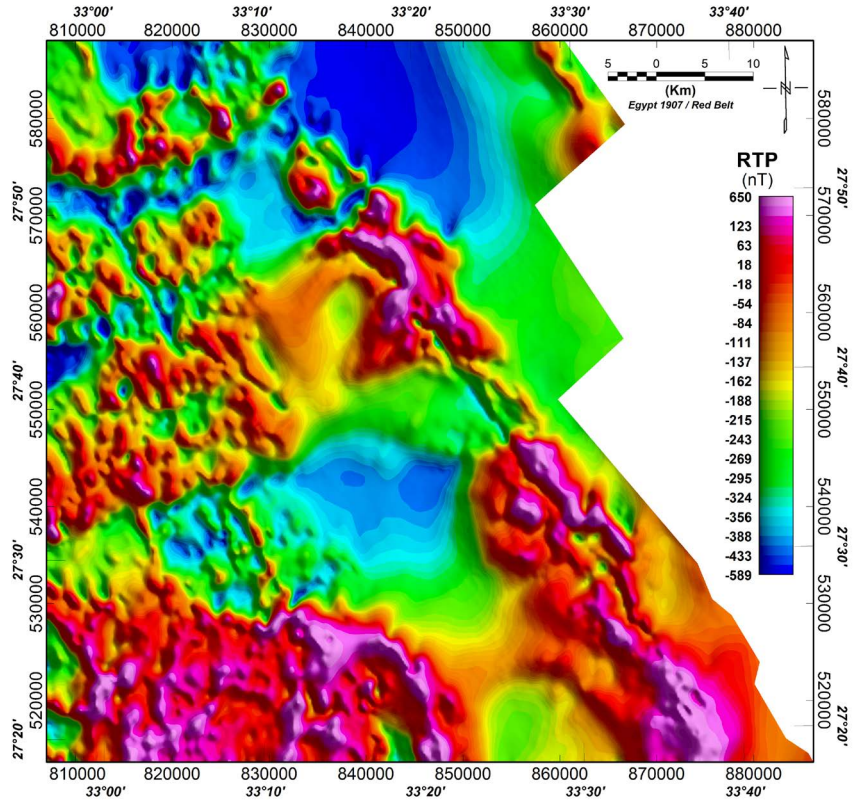

Figure 4. Reduced to magnetic pole (RTP) map of the study area.

The main purpose of using magnetic data in this work is to determine the geological structures that govern the mineralization process present in the area. Several techniques for detecting edges of magnetic source have been introduced such as: total horizontal derivative [33], analytic signal ([34] [35]) and tilt angle derivative [36].

Total horizontal derivative (THD) depends on the fact that the amplitude of the horizontal derivative of the RTP magnetic field resulted from a tabular body has the greatest values over the anomaly edges in case of vertical edges and well-separated edges from each other [33]. The method can be used to delineate the trends of subsurface fault [37]. It is less sensitive to noise and very strong in detection magnetic sources at shallow depths [38].

The analytic signal (AS) is a widely used tool to determine the geometry of the magnetic source [39]. The amplitude of the AS has a bell-shaped anomaly and lies above the causative magnetic source with maximum values corresponding to the edges of the source [40]. The AS method is independent of the source's magnetization; therefore, it is very useful in regions of rocks that have remnant magnetization [41].

In noisy data, tilt derivative (TD) techniques very powerful edge detector and responds equally well for both shallow- and deep-seated magnetic sources because it elaborates like an automatic gain-control filter [42]. Due to the nature of the arctangent trigonometric function, TD amplitude has a range of $-\pi/2$ and $+\pi/2$. Moreover, the amplitude of the TD has three rates: positive over the magnetic body, zero at/close to the body's edges, and negative elsewhere ([39] [43]). The three techniques (THD, AS & TD) were used to figure out the trends affecting the study area and, consequently, the mineralization process. These techniques and their result were presented in **Figure 5**.

3.2. Radio-Spectrometric Data

The qualitative interpretation of the airborne gamma-ray spectrometric data depends mainly upon the excellent correlation between the general pattern of the recorded measurements and the surface distribution of rock units. The texture of the radio-spectrometric contour lines (signatures) could be an aid during interpretation of surface geology (lithology and structure) [44].

The main four windows of radio-spectrometric data were gridded using suitable grid cell size and presented in **Figures 6-9**. Total Count map (TC) (**Figure 6**) for the area ranges from 0.0 to 22.76 μR/h. the highest readings are related to younger granites (gβ) which located at the NW, SW parts (Red Sea hills), at the eastern part (Esh El-mallaha range) and at NE corner (G. Zeit) trending mainly in NW-SE direction and partially in NE-SW direction.

Potassium map (**Figure 7**) show up the distribution of Potassium concentrations in the study area which resemble to great extent the distribution of TC concentrations. The concentrations of equivalent uranium range from 0.0 to 17.28 ppm (**Figure 8**). The highest values related mainly with younger granites (gβ) at the western part and Duwi formation (Kuw) at Esh El-mallaha range and

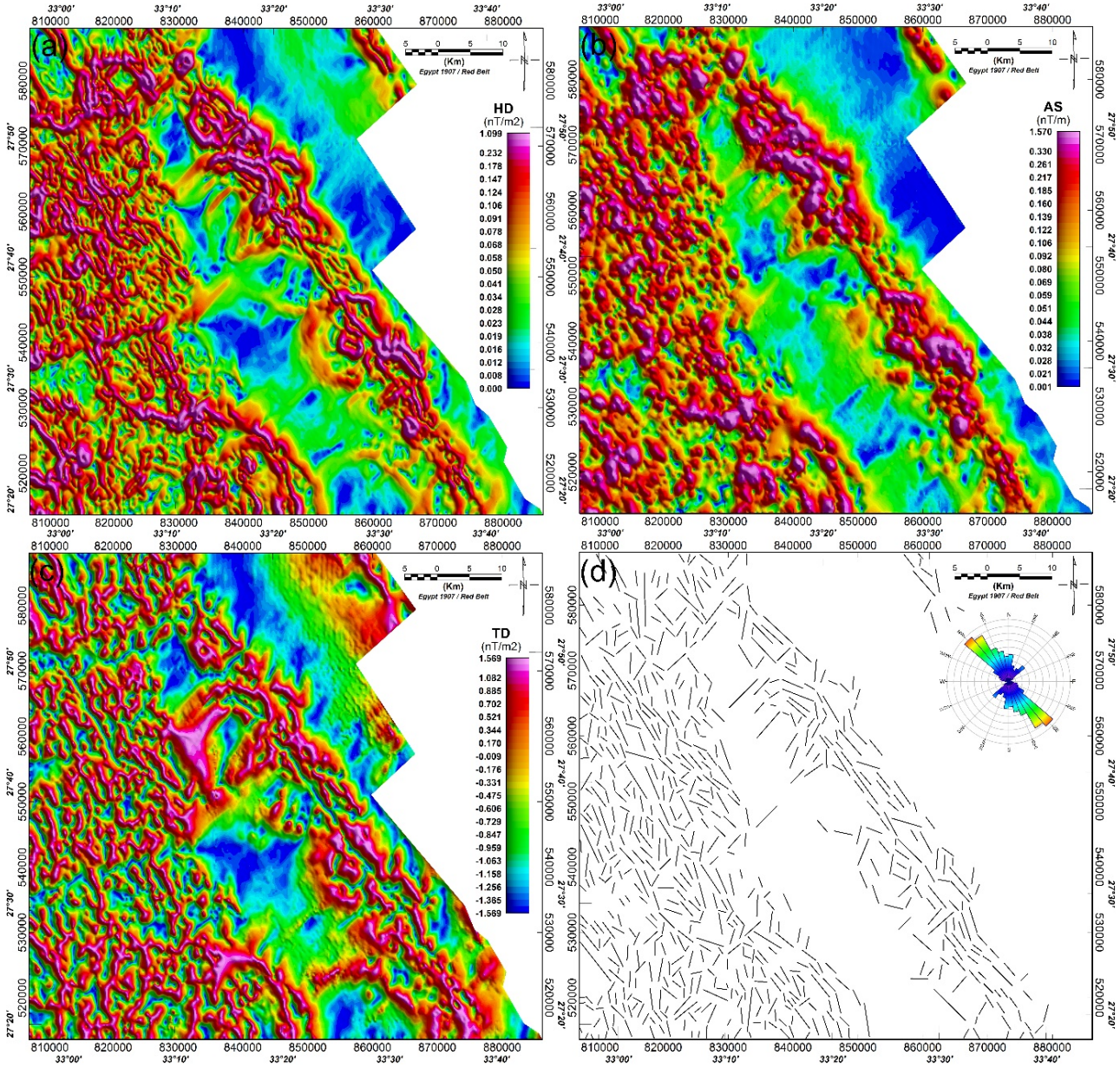

Figure 5. (a) Total horizontal derivative, (b) Analytic signal, (c) Tilt derivative of RTP data, and (d) the resulted lineation and its rose diagram.

partially with parts of older granites (g*α*). Equivalent thorium map is also presented in **Figure 9** with values reach about 40.64 ppm. Like as the aforementioned maps (**Figures 6-8**), the distribution of high values of equivalent thorium is also related mainly to the younger granitic rocks at the western part of the study area.

Different rock types have different characteristic concentrations of potassium, uranium, and thorium. Therefore, concentrations calculated from gamma-ray spectrometric data can be used to identify zones of consistent lithology and contacts between constraining lithologies [45]. The radioelements composite image (**Figure 10**) of the study area shows the variations occurring in the three

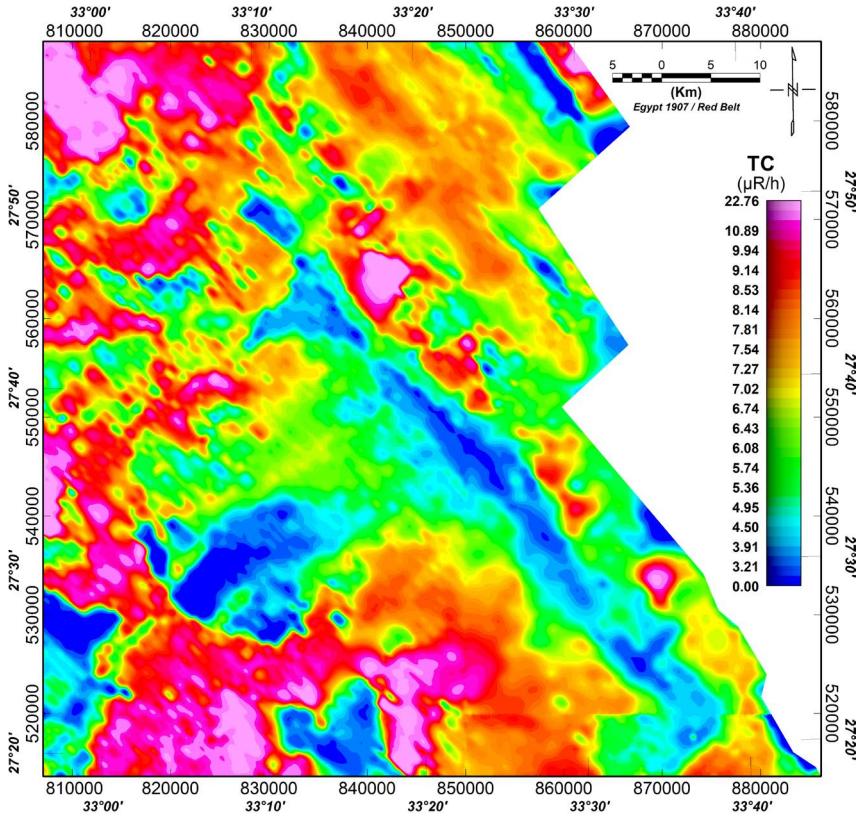

Figure 6. Total count (TC) map of the study area.

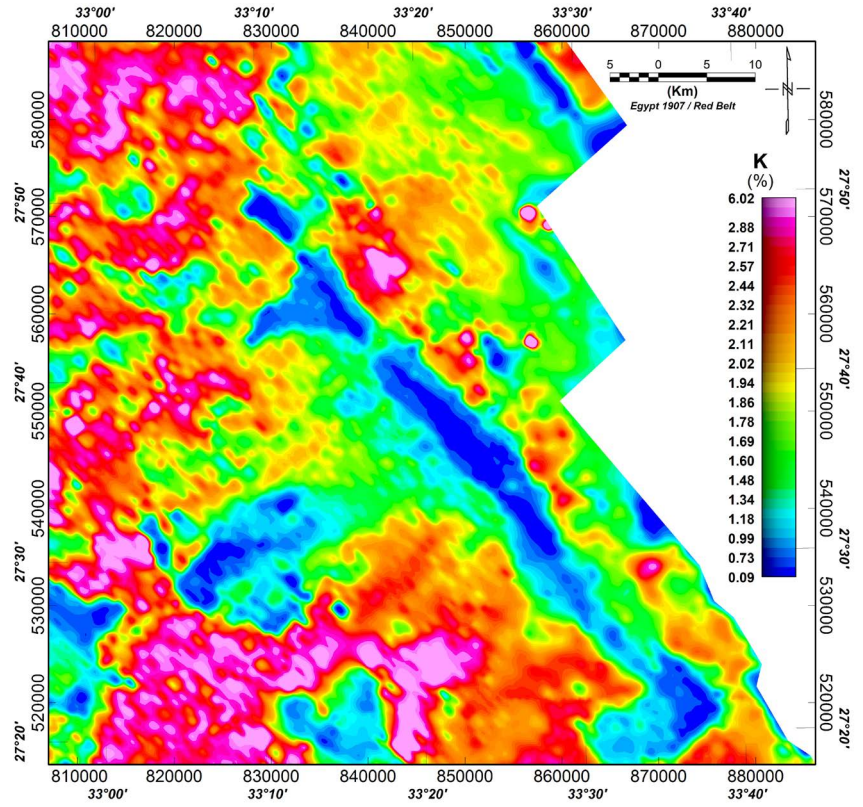

Figure 7. Potassium (K) map of the study area.

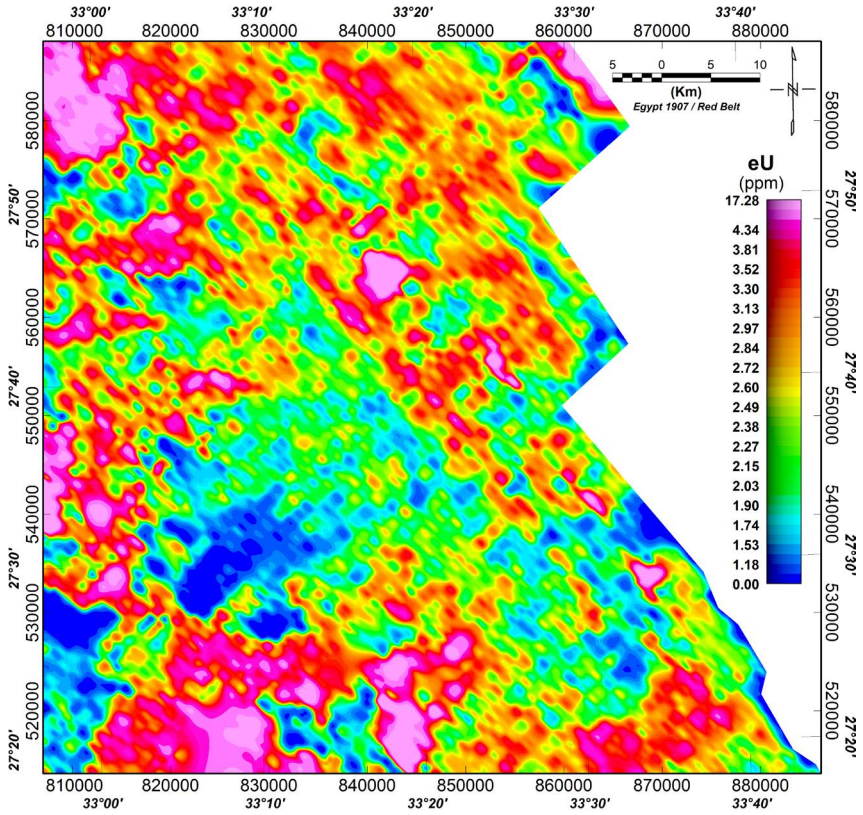

Figure 8. Equivalent uranium (eU) map of the study area.

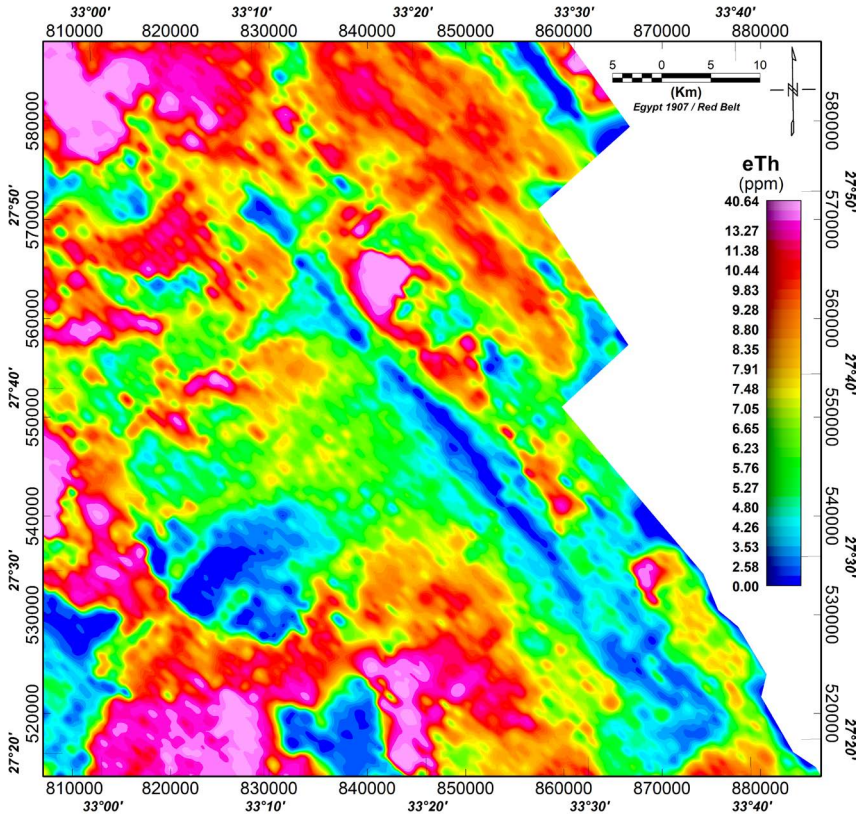

Figure 9. Equivalent Thorium (eTh) map of the study area.

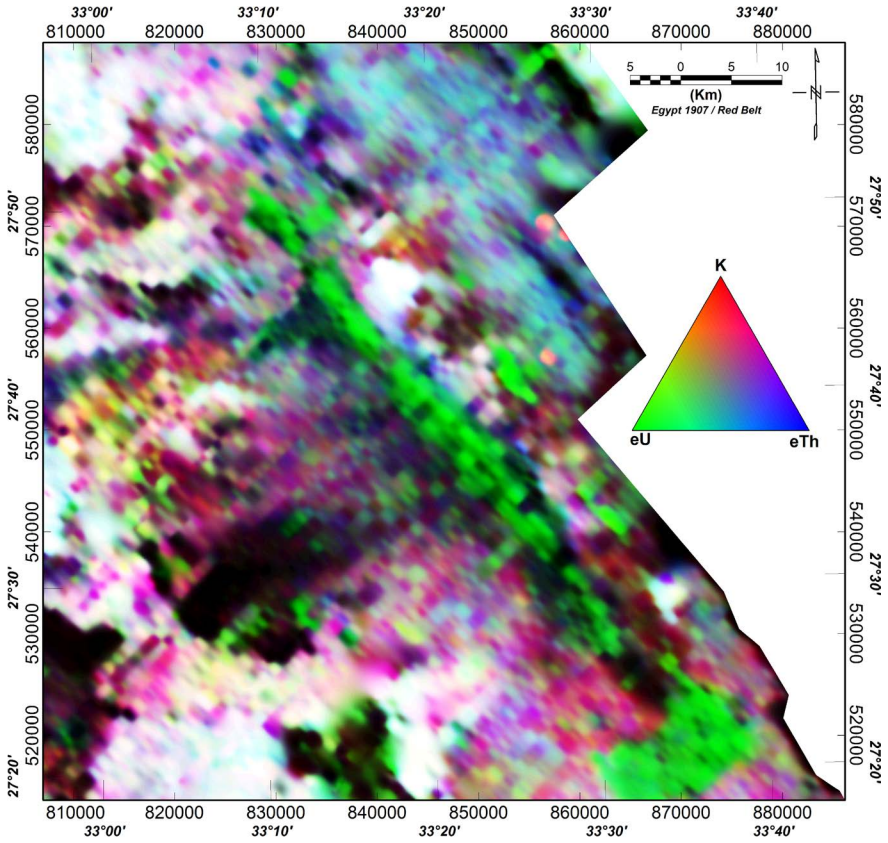

Figure 10. Radioelement composite image of the study area.

radioelements concentrations, which mainly reflect lithologic variations. It was noticed that the higher bright zones are clearly correlated with younger granite rocks which are normally characterized by their strong radio-spectrometric responses and elemental differences. Meanwhile, the ternary composite image shows dark areas of weak radioelement contents as indicative to the low radioactive rocks. The other remarkable notice is that the green colour which represents 100% of uranium concentration is well coincidence with Duwi formation at Esh El-mallaha range.

The same as radioelement composite image (Figure 10), uranium composite image (Figure 11) was constructed using eU in red, eU/K ratio in green and eU/eTh ratio in blue. The bright white means that the concentrations of eU, eU/K and eU/eTh are the highest at these parts, consequently, highest uranium concentrations. The bright white spots which indicate the highest concentrations of uranium are well correlated with Duwi formation, Dakhla formation and parts of Umm Mahara formation at Esh El-mallaha range. The black spots represent the lowest uranium concentrations all over the area.

3.3. Remote Sensing Data

The main objective of remote sensing data is defining areas of hydrothermal alterations and extracting the surface lineaments which affect the study area. Using band composite 7, 5, 3 in R, G, and B discriminates between felsic, mafic and

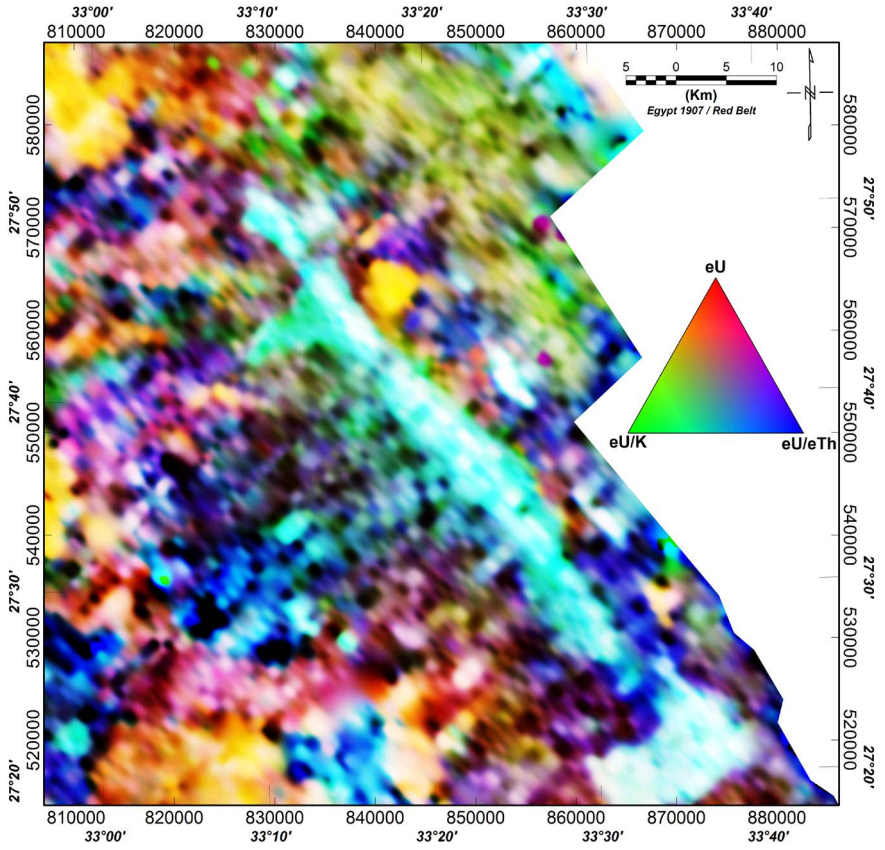

Figure 11. Equivalent uranium composite image of the study area.

wadi deposits. In this combination, the felsic varieties appear in reddish brown color, the mafic rocks are dark; however, the wadi deposits show bright tone (Figure 12).

Band ratio is widely used in mineralization to improve the spectral characteristics of the alteration regions depending on the absorption bands of their altered minerals. For example, using Landsat-7 the iron bearing (ferrous and ferric oxides) minerals are delineated using band ratios 3/5 and 5/4 [46] and 3/1 [47]. Moreover, band ratio 5/7 was applied to detect high values of the hydroxyl-bearing minerals (kaolinite, alunite, muscovite, epidotes and chlorites) [48]. The hydrothermal alteration areas are clearly highlighted in bright tone by applying the band ratio 6/7 of Landsat-8 OLI that equal to 5/7 of Landsat-7 ETM+ (Figure 13(a)). In order to highlight the alteration areas using band ratio composites 6/7, 6/5, 5 in R, G, and B, ([16] [49]) the alteration areas clearly marked in yellow color (Figure 13(b)).

Band ratio 5/4 was used for detecting the alteration zone of ferrous and ferric minerals in the study area as shown in Figure 14(a) in which these alteration areas are represented by the very clear white color surrounded by the grey color. For detecting the Alteration zone of the hydroxyl (OH)-bearing minerals, the band ratio 5/7 is used, as shown in Figure 14(b). Another band ratio has been applied for representing the final alteration zone in the study area, this band ra-

tion displayed the OH-bearing menials (5/7 ratio) in R, the Fe-bearing menials (5/4 ratio) in B and OH + Fe (5/7 + 5/4) in G (Figure 15), which appear in very light pink colour.

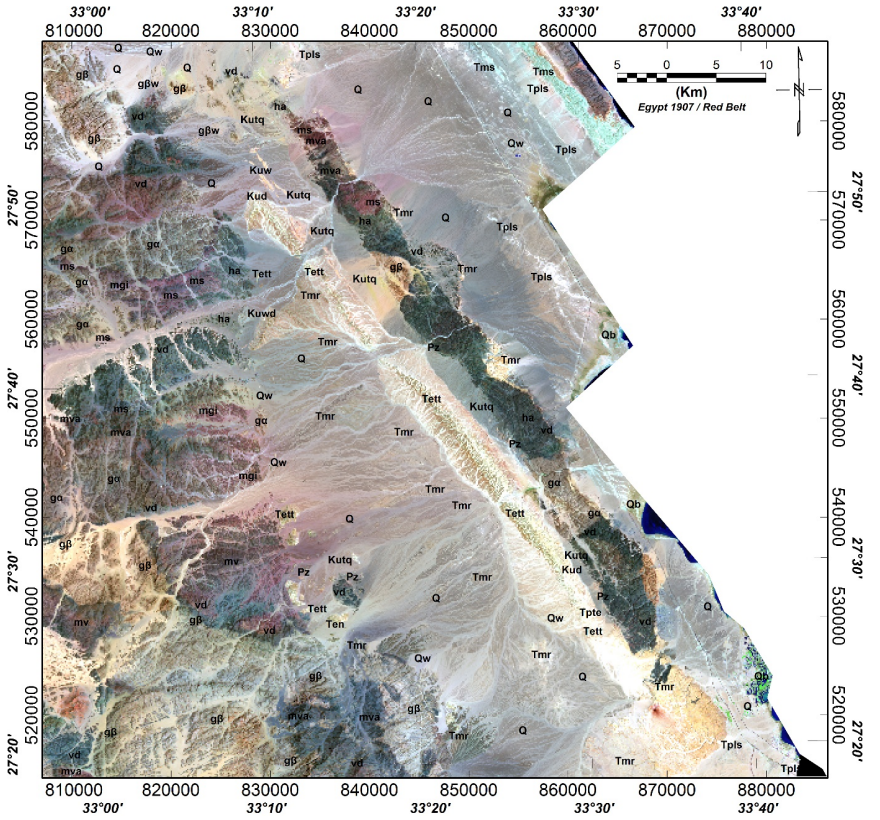

Figure 12. Landsat-8 composite image 7, 5, 3 in R, G, and B.

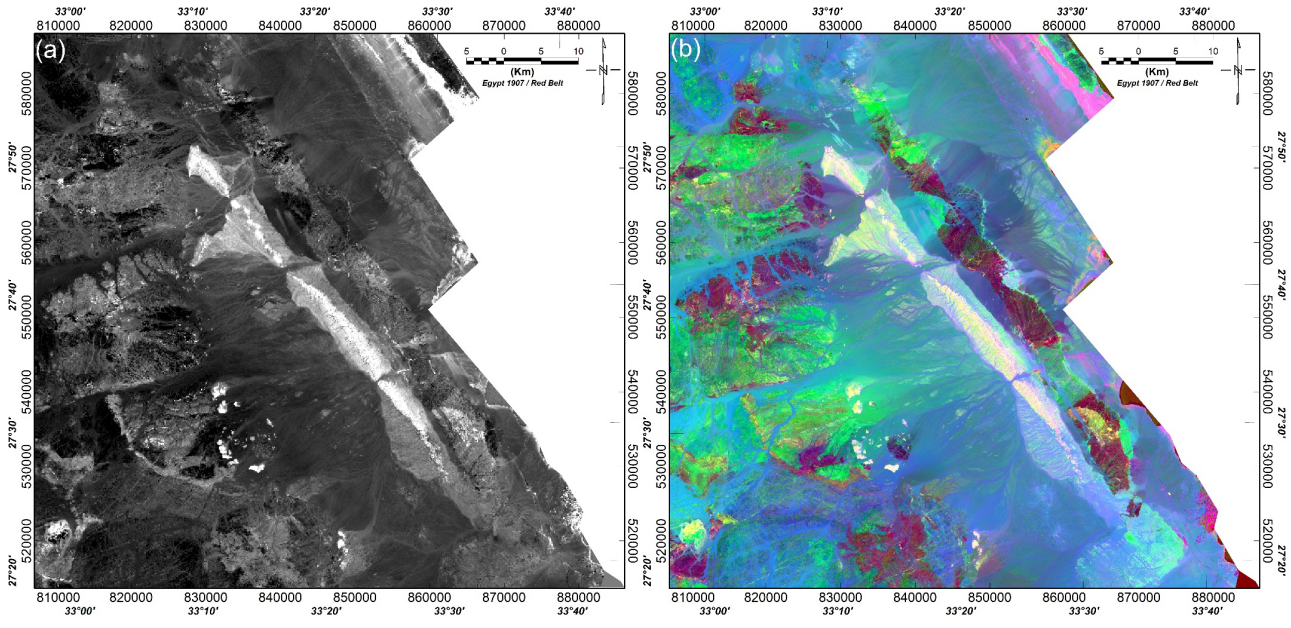

Figure 13. (a) Band ratio 6/7 of Landsat-8, (b) 6/7, 6/5, 5 in R, G, and B composite image reveals the alteration areas in yellow colour.

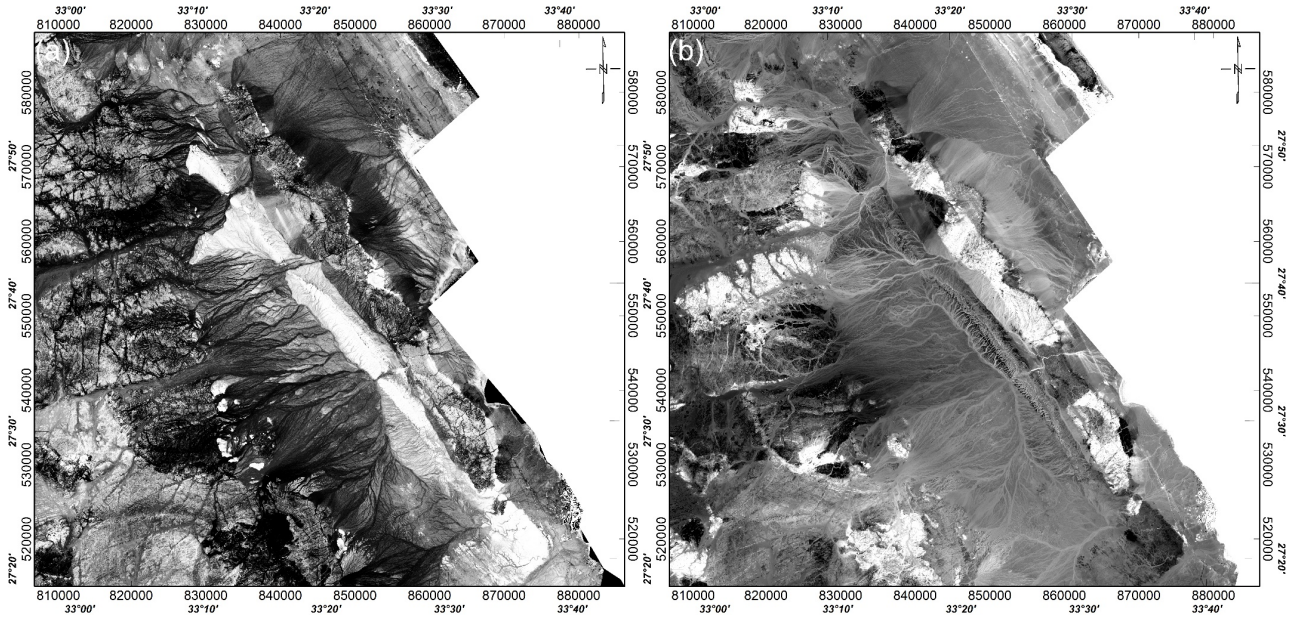

Figure 14. (a) Band ratio 5/4 of Landsat-8 (Fe-minerals, (b) Band ratio 5/7 of Landsat-8 (OH-bearing minerals).

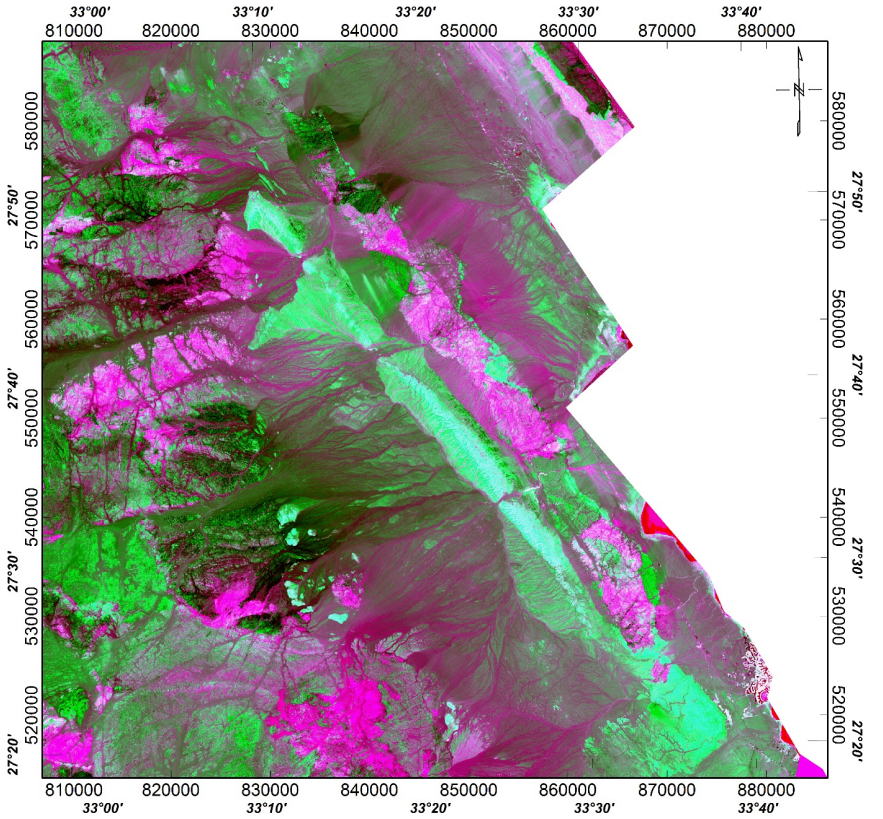

Figure 15. Band ratio image showing the alteration areas of ore deposits mineralization represented with very light pink color after displaying OH in (R), Fe in (B) and OH + F in (G).

4. Data Interpretation

The main aim of this research work is to deduce radioactive mineralization, es-

pecially uranium promising areas, determine the alteration zones which related to mineralization accumulation and geologic structure trends affecting the study area. The integration between the geophysical data (magnetic and radio-spectrometry) and remote sensing data is a good tool for delineating and interpreting the objectives of the study.

4.1. Geologic Structure Trends

The different geological structures that affect the study area is one of the most important factors that affect the mineralization accumulation. Magnetic method is very valuable tool to delineate the subsurface structure and basement configuration. In this work, the subsurface structure trends (deep and shallow trends) were delineated through magnetic method by using the edge detectors (THD, AS and TD) and presented in **Figure 5**.

In addition to subsurface structure trends deduced from magnetic method, Landsat-8 satellite data and their analyzed images are very effective for lineaments mapping (e.g.: [50] [51] [52]). The Landsat 8 structure lineaments deduced by using automatic extraction using the LINE tool in PCI Geomatica 2013 software. This algorithm improves the data edges through specific parameters as edge detection, thresholding, and curve extraction (e.g. [53]).

In the current study, the line density map was resulted using the ArcMap line density tool; it shows the frequency of lineaments per unit area. The density map technique was applied to the lineaments determined by the geology, magnetic and satellite image and presented in **Figures 16-18** respectively, to give a comprehensive sight to the structure trends affecting the study area.

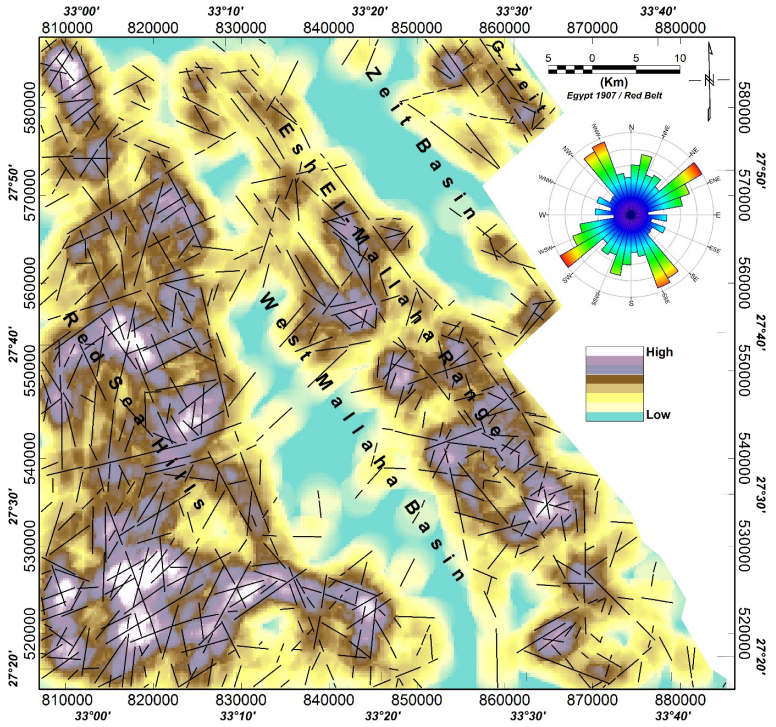

Figure 16. Geologic lineation on density geologic lineaments map with its rose diagram.

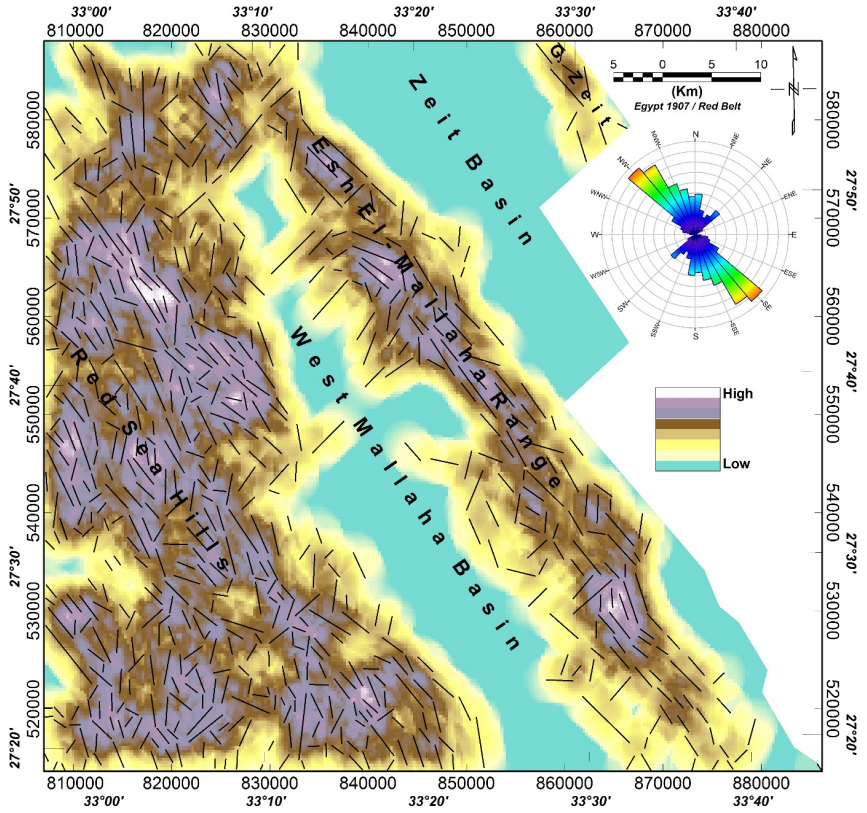

Figure 17. Magnetic lineation on density magnetic lineaments map with its rose diagram.

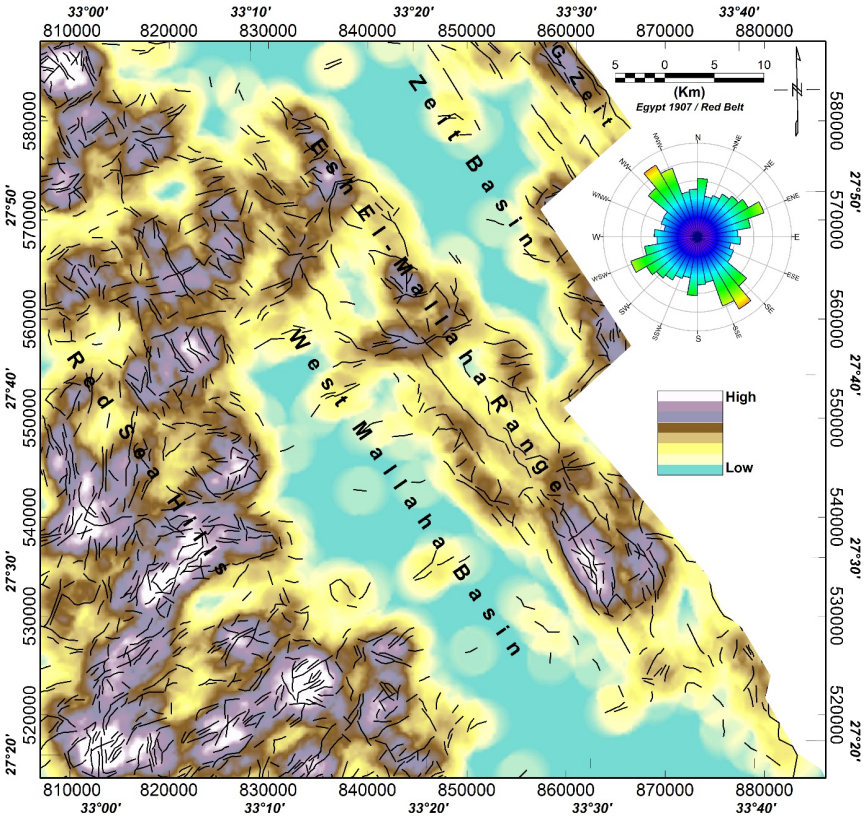

Figure 18. Satellite image lineation on density lineaments map with its rose diagram.

Figures 16-18 show that the higher densities reflect the topographic variation for the exposed lithological units, thus it indicates that the basement and sedimentary rocks in this area are highly deformed. The three density maps (Figures 16-18) clarify that the basement at the western part of the study area (Red Sea hills) are highly dissected with normal faults. In addition, Esh El-mallaha range at the eastern part and G. Zeit at NE part of the study area were affected by normal faults. The three maps also show that Red Sea hills, Esh El-Mallaha range and G. Zeit structures inclosing West Mallaha basin and Zeit basin. The rose diagram of the three maps (Figures 16-18) show that NW-SE direction is the predominance trend in the study area whereas NE-SW trend appeared in geologic structure lineaments. In addition, lineation density map of satellite image (Figure 18) showed the presence of ENE-WSW trend.

4.2. Uranium Anomalies and Alteration Zones

The main target of aerial prospection using gamma ray spectrometric survey data is the delineation of expected boundaries of radioactive concentrations, in which the varying rock units are enriched in eU, eTh and K [54]. Because uranium is the most important radioactive element; so, in this research work, uranium anomalies will be determined using radio-spectrometric data depending on the uranium composite image (Figure 11). The bright white spots on the uranium composite image represent the highest values of uranium enrichment.

The integration between the uranium composite image (Figure 11) and alteration map deduced from satellite image band ratio 6/7 (Figure 13(a)) is presented in Figure 19. The first look to Figure 19 shows that the uranium enrichment parts on uranium composite image (Figure 17(a)) are well correlated with

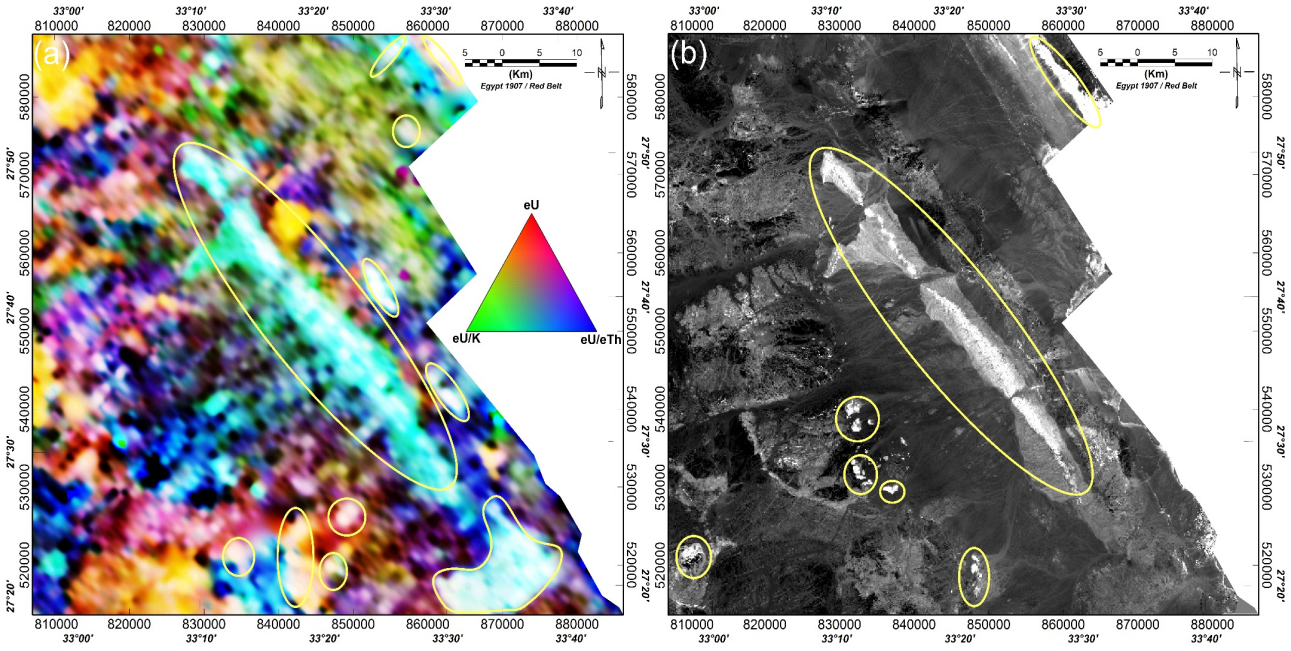

Figure 19. Integration between (a) uranium composite image, (b) band ratio 6/7 of Landsat 8.

the alteration zones detected on alteration map (Figure 19(b)). The main uranium enrichment and alteration zone is related with Esh El-Mallaha range, especially with Duwi formation. In addition, there are other parts related to Umm Mahara formation located at the SE part of the study area. There are other small parts enriched with uranium and related with younger granites. The alteration zone map (Figure 19(b)) clarifies that there are other altered rocks at NE part related to Umm Gheig formation, small parts related to Thebes formation at the boundary of basement rocks and parts of Dokhan volcanics to the west (Red Sea hills).

4.3. Basement Tectonic and Uranium Anomalies

The magnetic data considered to be a very good direct method to detect the basement configuration. The integration between the basement structure and uranium anomalies was introduced in Figure 20. The figure shows clearly that most of uranium anomalies were related mainly to faults in NW-SE direction. The structure produced from basement tectonic map is well correlated with structure trends produced from Figures 16-18 that NW-SE is the most predominance trend all over the study area at different depth levels, and these faults related mainly with uranium anomalies. Consequently, the uranium anomalies are not only controlled by the difference in rock properties but also by structure.

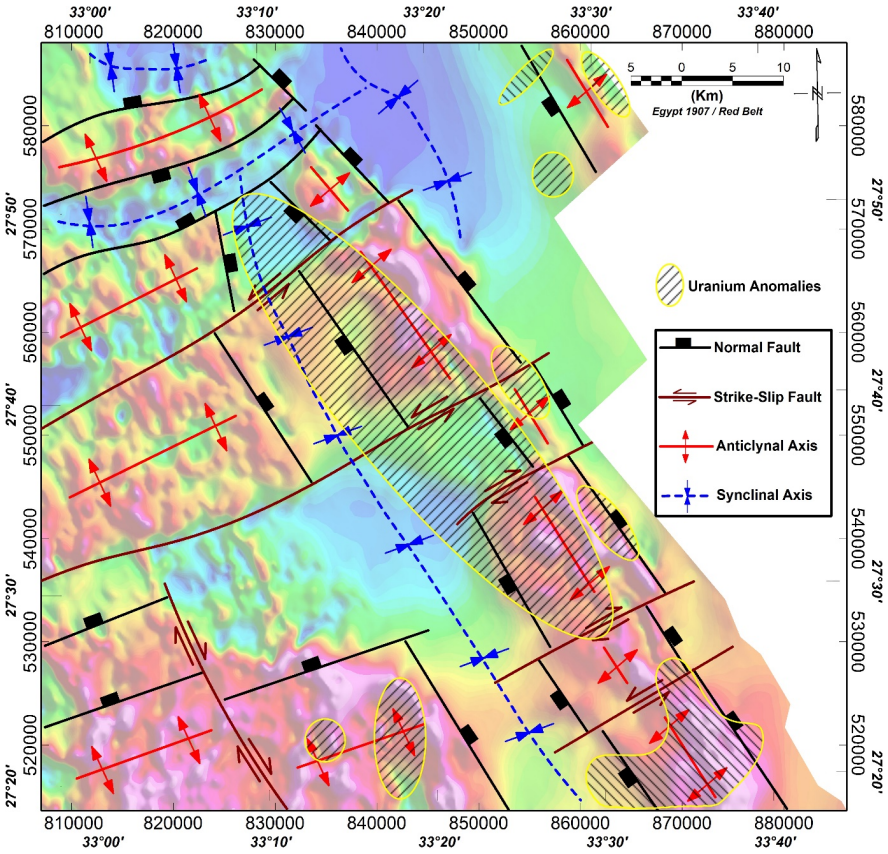

Figure 20. Integrated map between basement tectonic and uranium anomalies.

5. Conclusions

This research deals essentially with three data sets to achieve three main objectives: structure trends affecting the study area, uranium anomalous areas and alteration zones. Airborne magnetic data were analyzed using edge detectors (THD, AS and TD) to detect the geologic structure trends affecting the study area. In addition, radio-spectrometry and Landsat image helped to determine the uranium anomalous areas and alteration zones.

By integration between the lineaments of geology, magnetic and Landsat image, NW-SE trend was found to be the most predominant trend all over the area. This integration also shows up that the basement (Red Sea hills), Esh El-mallaha range and G. Zeit are confining two large basins (West Mallaha and Zeit).

In addition, the integration between uranium composite image (spectrometry data) and alteration map (band ratio 6/7 image of Landsat 8 data) clarifies that the main areas of uranium enrichment (Duwi formation at Esh El-Mallaha range) are well correlated to alteration zones. Basement tectonic map shows that uranium anomalies are controlled by structures mainly in NW-SE direction.

Acknowledgements

Many thanks to all my colleagues at the Airborne Geophysics Department of Nuclear Materials Authority, especially to Prof. Alaa Aref who advises me more one time in all my papers.

Conflicts of Interest

The author declares no conflicts of interest regarding the publication of this paper.

References

[1] Abdel Hafeez, Th.H., Youssef, M.A.S. and Mohamed, W.H. (2015) Engineering Utilization of Airborne Gamma Ray Spectrometric Data for Geological Mapping and Radioactive Mineral Exploration of Gabel Umm Tineidba Area, Southeastern Desert, Egypt. *World Journal of Engineering*, **12**, 149-160. https://doi.org/10.1260/1708-5284.12.2.149

[2] Minty, B. and FitzGerald, D. (2015) Developments in Airborne Gamma-Ray Spectrometry to Aid the Search for Strategic Minerals. *KEGS Symposium* 2015 "*Exploration for Strategic Minerals*", Toronto, 28 February 2015, 1-5.

[3] Ahmed, S.B. (2018) Integration of Airborne Geophysical and Satellite Imagery Data to Delineate the Radioactive Zones at West Safaga Area, Eastern Desert, Egypt. *NRIAG Journal of Astronomy and Geophysics*, **7**, 297-308. https://doi.org/10.1016/j.nrjag.2018.07.005

[4] Bishta, A.Z. (2013) Utilities of Landsat 7 Data and Selective Image Processing in Characterization of Radioactivity Zones of Wadi Baba-Wadi Shalal Area, Westcentral Sinai, Egypt. *Arabian Journal of Geosciences*, **6**, 3513-3526. https://doi.org/10.1007/s12517-012-0595-5

[5] Pour, A.B., Park, Y., Park, T.Y.S., Hong, J.K., Hashim, M., Woo, J. and Ayoobi, I. (2018) Regional Geology Mapping Using Satellite-Based Remote Sensing Approach

in Northern Victoria Land, Antarctica. *Polar Sciences*, **16**, 23-46. https://doi.org/10.1016/j.polar.2018.02.004

[6] Chattoraj, S.L., Prasad, G., Sharma, R.U., Champatiray, P.K., Van der Meer, F.D., Guha, A. and Pour, A.B. (2020) Integration of Remote Sensing, Gravity, and Geochemical Data for Exploration of Cu-Mineralization in Alwar Basin, Rajasthan, India. *International Journal of Applied Earth Observation and Geoinformation*, **91**, Article ID: 102162. https://doi.org/10.1016/j.jag.2020.102162

[7] Sroor, A., El-Bahi, S.M., Ahmed, F. and Abdel-Haleem, A.S. (2002) Natural Radioactivity and Radon Exhalation Rate of Soil in Southern in Egypt. *Applied Radiation and Isotopes*, **55**, 873-879. https://doi.org/10.1016/S0969-8043(01)00123-3

[8] Ramsay, J.G. and Huber, M.I. (1987) The Techniques of Modern Structural Geology. In: *Folds and Fractures*, Vol. 2, Academic Press, London, 391 p.

[9] Sabin's, F.F. (1997) Remote Sensing; Principals and Interpretation. Fourth Edition, Freeman, San Francisco, 449.

[10] Goetz, A.F.H., Rock, B.N. and Rowan, L.C. (1983) Remote Sensing for Exploration: An Overview. *Economic Geology*, **78**, 573-590. https://doi.org/10.2113/gsecongeo.78.4.573

[11] Rowan, L.C., Kingstone, M.J. and Crowley, J.K. (1986) Spectral Reflectance of Carbonatite and Related Alkalic Igneous Rocks for Four North American Localities. *Economic Geology*, **81**, 857-871. https://doi.org/10.2113/gsecongeo.81.4.857

[12] Abrams, M. and Hook, S.J. (1985) Simulated Aster Data for Geologic Studies. *IEEE Transactions on Geoscience and Remote Sensing*, **33**, 692-699. https://doi.org/10.1109/36.387584

[13] Okada, K., Segawa, K. and Hayashi, I. (1993) Removal of the Vegetation Effect from LANDSAT TM and GER Imaging Spectroradiometer Data. *ISPRS Journal of Photogrammetry and Remote Sensing*, **48**, 16-27. https://doi.org/10.1016/0924-2716(93)90052-O

[14] Amuda, O.S., Adebisi, S., Jimoda, L. and Alade, A. (2014) Challenges and Possible Panacea to the Municipal Solid Wastes Management in Nigeria. *Journal of Sustainable Development Studies*, **6**, 64-70.

[15] Poormirzaee, R. and Oskouei, M.M. (2010) Use of Spectral Analysis for Detection of Alterations in ETM Data, Yazd, Iran. *Applied Geomatics*, **2**, 147-154. https://doi.org/10.1007/s12518-010-0027-8

[16] Ramadan, T.M., Abdelsalam, M.G. and Stern, R.J. (2001) Mapping Gold-Bearing Massive Sulfide Deposits in the Neoproterozoic Allaqi Suture, Southeast Egypt with Landsat TM and SIR-C/X SAR Images. *Photogrammetric Engineering & Remote Sensing*, **67**, 491-497.

[17] Mia, M.B. and Fujimitsu, Y. (2012) Mapping Hydrothermal Altered Mineral Deposits Using Landsat 7 ETM+ Image in and around Kuju Volcano, Kyushu, Japan. *Journal of Earth System Science*, **121**, 1049-1057. https://doi.org/10.1007/s12040-012-0211-9

[18] Sabin's, F.F. (1999) Remote Sensing for Mineral Exploration. *Ore Geology Reviews*, **14**, 157-183. https://doi.org/10.1016/S0169-1368(99)00007-4

[19] Aydal, D., Ardal, E. and Dumanlilar, O. (2007) Application of the Crosta Technique for Alteration Mapping of Granitoidic Rocks Using ETM+ Data: Case Study from Eastern Tauride Belt (SE Turkey). *International Journal of Remote Sensing*, **28**, 3895-3913. https://doi.org/10.1080/01431160601105926

[20] Liu, J.P., Song, M., Horton, R.M. and Hu, Y. (2013) Reducing Spread in Climate

Model Projections of a September Ice-Free Arctic. *Proceedings of the National Academy of Sciences of the United States of America*, **110**, 12571-12576. https://doi.org/10.1073/pnas.1219716110

[21] Tangestani, M.H. and Moore, F. (2000) Iron Oxide and Hydroxyl Enhancement Using the Crosta Method: A Case Study from the Zagros Belt, Fars Province, Iran. *The International Journal of Applied Earth Observation and Geoinformation*, **2**, 140-146. https://doi.org/10.1016/S0303-2434(00)85007-2

[22] Holden, E.J., Fu, S.C., Kovesi, P., Dentith, M., Bourne, B. and Hope, M. (2011) Automatic Identification of Responses from Porphyry Intrusive Systems within Magnetic Data Using Image Analysis. *Journal of Applied Geophysics*, **74**, 255-262. https://doi.org/10.1016/j.jappgeo.2011.06.016

[23] Gay Jr., S.P. (1972) Fundamental Characteristics of Aeromagnetic Lineaments, Their Geological Significance, and Their Significance to Geology. The New Basement Tectonics' American Stereo Map Company, Salt Lake City, 94 p.

[24] Stern, R.T. and Hedge, C.E. (1985) Geochronologic and Isotopic Constrains on Late Precambrian Crustal Evaluation in the Eastern Desert of Egypt. *American Journal of Science*, **285**, 97-127. https://doi.org/10.2475/ajs.285.2.97

[25] Shackleten, R.M., Ries, A.C., Grahm, R.H. and Fitches, W.R. (1980) Late Precambrian Ophiolitic Mélange in the Eastern Desert of Egypt. *Nature*, **285**, 472-474. https://doi.org/10.1038/285472a0

[26] Aboud, E., Mekkawi, M. and Khalil, A. (2006) Interpretation of Aeromagnetic Data of Esh El Mellaha Area, Gulf of Suez, Egypt. *NRIAG Journal of Geophysics*, Special Issue, 45-58.

[27] Dardir, A.A. and Abu Zeid, K.M. (1972) Geology of the Basement Rocks between Latitudes 27 00 and 27 30 N, Eastern Desert. *Annals of the Geological Survey of Egypt*, **2**, 129-159.

[28] Essawy, M.A. and Abu Zeid, K.M. (1972) Atalla Felsite Intrusion and Its Neighboring Flows and Tuffs, Eastern Desert. *Annals of the Geological Survey of Egypt*, **2**, 271-280.

[29] Said, R. (1962) Geology of Egypt. Elsevier Publ. Co., Amsterdam and New York, 293-319.

[30] AeroService (1984) Final Operational Report of Airborne Magnetic/Radiation Survey in the Eastern Desert, Egypt, for the Egyptian General Petroleum Corporation: AeroService Division, Houston, Texas, 1984, Six Volumes. Western Geophysical Company of America.

[31] Dobrin, M.B. (1976) Introduction to Geophysical Prospecting. McGraw-Hill Book Company, New York, 630 p.

[32] Ibraheem, I.M., Gurk, M., Tougiannidis, N. and Tezkan, B. (2018) Subsurface Imaging of the Neogene Mygdonian Basin, Greece Using Magnetic Data. *Journal of Pure and Applied Geophysics*, **175**, 2955-2973. https://doi.org/10.1007/s00024-018-1809-x

[33] Cordell, L. and Grauch, V.J.S. (1985) Mapping Basement Magnetization Zones from Aeromagnetic Data in the San Juan Basin, New Mexico. In: Hinzc, W.J., Ed., *The Utility of Regional Gravity and Magnetic Anomaly Maps*, Society of Exploration Geophysicists, Tulsa, 181-197. https://doi.org/10.1190/1.0931830346.ch16

[34] Nabighian, M.N. (1972) The Analytic Signal of Two-Dimensional Magnetic Bodies with Polygonal Cross-Section: Its Properties and Use for Automated Anomaly Interpretation. *Geophysics*, **37**, 507-517. https://doi.org/10.1190/1.1440276

[35] Roest, W.R., Verhoef, J. and Pilkngton, M. (1992) Magnetic Interpretation Using the 3-D Analytic Signal. *Geophysics*, **57**, 116-125. https://doi.org/10.1190/1.1443174

[36] Cooper, G.R.J. and Cowan, D.R. (2006) Enhancing Potential Field Data Using Filters Based on the Local Phase. *Computers & Geosciences*, **32**, 1585-1591. https://doi.org/10.1016/j.cageo.2006.02.016

[37] Grant, F.S. and West, G.F. (1965) Interpretation Theory in Applied Geophysics. McGraw-Hill, New York.

[38] Phillips, J.D. (2002) Processing and Interpretation of Aeromagnetic Data for the Santa Cruz Basin-Patahonia Mountains Area, South-Central Arizona. U.S. Geological Survey Open-File Report 02-98, U.S. Geological Survey, Reston. https://doi.org/10.3133/ofr0298

[39] Miller, H.G. and Singh, V. (1994) Potential Field Tilt—A New Concept for Location of Potential Field Sources. *Journal of Applied Geophysics*, **32**, 213-217. https://doi.org/10.1016/0926-9851(94)90022-1

[40] Al-Ibiari, M.G., Ismail, A.A., El-Khafeef, A.A., Basheer, A.A., El-laban, A.M. and Tarek, Y. (2018) Analysis and Interpretation of Aeromagnetic Data for Wadi Zeidun Area, Central Eastern Desert, Egypt. *Egyptian Journal of Petroleum*, **27**, 285-293. https://doi.org/10.1016/j.ejpe.2017.04.002

[41] Brethes, A., Guarnieri, P., Rasmussen, T.M. and Bauer, T.E. (2018) Interpretation of Aeromagnetic Data in the Jameson Land Basin, Central East Greenland: Structures and Related Mineralized Systems. *Tectonophysics*, **724-725**, 116-136. https://doi.org/10.1016/j.tecto.2018.01.008

[42] Arisoy, M. and Dikmen, Ü. (2013) Edge Detection of Magnetic Sources Using Enhanced Total Horizontal Derivative of the Tilt Angle. *Bulletin of the Earth Sciences Application and Research Centre of Hacettepe University*, **34**, 73-82.

[43] Ibraheem, I.M., Haggag, M. and Tezkan, B. (2019) Edge Detectors as Structural Imaging Tools Using Aeromagnetic Data: A Case Study of Sohag Area, Egypt. *Geosciences*, **9**, Article No. 211. https://doi.org/10.3390/geosciences9050211

[44] International Atomic Energy Agency (IAEA) (1979) Gamma-Ray Surveys in Uranium Exploration. Technical Report Series 186, Vienna.

[45] Elkhadragy, A.A., Ismail, A.A., Eltarras, M.M. and Azzazy, A. (2016) Utilization of Airborne Gamma Ray Spectrometric Data for Radioactive Mineral Exploration of G.Abu Had—G.Umm Qaraf Area, South Eastern Desert, Egypt. *NRIAG Journal of Astronomy and Geophysics*, **6**, 148-161. https://doi.org/10.1016/j.nrjag.2016.12.001

[46] Sultan, M., Arvidson, R.E. and Sturchio, N.C. (1986) Mapping of Serpentinites in the Eastern Desert of Egypt by Using Landsat Thematic Mapper Data. *The Journal of Geology*, **14**, 995-999. https://doi.org/10.1130/0091-7613(1986)14<995:MOSITE>2.0.CO;2

[47] Abrams, M.J., Brown, D., Lepley, L. and Sadowski, R. (1983) Remote Sensing for Porphyry Copper Deposits in Southern Arizona. *Economic Geology*, **78**, 591-604. https://doi.org/10.2113/gsecongeo.78.4.591

[48] Gupta, R.P. (2003) Remote Sensing Geology. 2nd Edition, Springer, Berlin. https://doi.org/10.1007/978-3-662-05283-9

[49] Ramadan, T.M. and Sultan, S.A. (2004) Integration of Remote Sensing, Geological and Geophysical Data for the Identification of Massive Sulphide Zones at Wadi Allaqi Area, South Eastern Desert, Egypt. Vol. 18, MERC, Ain Shams University, Cairo, 165-174.

[50] Marghany, M. and Hashim, M. (2010) Lineament Mapping Using Multispectral

Remote Sensing Satellite Data. *International Journal of Physical Sciences*, **5**, 1501-1507. https://doi.org/10.3923/rjasci.2010.126.130

[51] Mwaniki, M.W., Moeller, M.S. and Schellmann, G. (2015) A Comparison of Landsat 8 (OLI) and Landsat 7 (ETM+) in Mapping Geology and Visualizing Lineaments: A Case Study of Central Region Kenya. *The International Archives of the Photogrammetry, Remote Sensing and Spatial Information Sciences*, **XL-7/W3**, 897-903. https://doi.org/10.5194/isprsarchives-XL-7-W3-897-2015

[52] Kamel, M., Youssef, M., Hassan, M. and Bagash, F. (2016) Utilization of ETM+ Landsat Data in Geologic Mapping of Wadi Ghadir-Gabal Zabara Area, Central Eastern Desert, Egypt. *The Egyptian Journal of Remote Sensing and Space Sciences*, **19**, 343-360. https://doi.org/10.1016/j.ejrs.2016.06.003

[53] Zoheir, B., Emam, A., Abdel-Wahed, M. and Soliman, N. (2019) Multispectral and Radar Data for the Setting of Gold Mineralization in the South-Eastern Desert, Egypt. *Remote Sensing*, **11**, Article No. 1450. https://doi.org/10.3390/rs11121450

[54] Saunders, D.F. and Potts, M.J. (1976) Interpretation and Application of High Sensitivity Airborne Gamma Ray Spectrometer Data. Exploration for Uranium Ore Deposits. Proc. Series. IAEA, Vienna.